

# Quantum Melting of Spin Ice: Emergent Cooperative Quadrupole and Chirality

Shigeki Onoda and Yoichi Tanaka

Condensed Matter Theory Laboratory, RIKEN, 2-1, Hirosawa, Wako 351-0198, Saitama, JAPAN  
(Dated: May 27, 2022)

A quantum melting of the spin ice is proposed for pyrochlore-lattice magnets  $\text{Pr}_2\text{TM}_2\text{O}_7$  ( $\text{TM} = \text{Ir}$ ,  $\text{Zr}$ , and  $\text{Sn}$ ). The quantum superexchange Hamiltonian having a nontrivial magnetic anisotropy is derived in the basis of atomic non-Kramers magnetic doublets. The ground states exhibit a cooperative ferroquadrupole and pseudospin chirality, forming a magnetic analog of smectic liquid crystals. Our theory accounts for dynamic spin-ice behaviors experimentally observed in  $\text{Pr}_2\text{TM}_2\text{O}_7$ .

PACS numbers: Valid PACS appear here

It has been a great challenge to realize unconventional spin-liquid states in three-dimensional magnets. It is achieved by preventing a dipole long-range order (LRO) of magnetic moments, which requires appreciable quantum spin fluctuations and geometrical frustration of magnetic interaction [1–4]. The importance of the geometrical frustration is manifest as in pyrochlore systems [5–8]. In particular, in the dipolar spin ice  $R_2\text{Ti}_2\text{O}_7$  ( $R = \text{Dy}$  or  $\text{Ho}$ ) [6–8], the rare-earth magnetic moment located at each vertex of tetrahedrons points either inwards (“in”) to or outwards (“out”) from the center (Fig. 1 (a)). The nearest-neighbor ferromagnetic coupling mainly due to the magnetic dipolar interaction favors macroscopically degenerate “2-in, 2-out” configurations without any LRO, forming a magnetic analog of the water ice [8]. Then, the classical spins are quenched into one of the degenerate ground states [9]. Usually, a thermal heating is required for melting the quenched spin ice. Here, we pursue an alternative possibility that quantum fluctuations melt the spin ice: the quantum entanglement among degenerate states lift the macroscopic degeneracy, suppress the spin-ice freezing, and lead to a distinct ground state.

A realistic approach to the quantum melting of the spin ice is to choose a rare-earth ion with fewer  $f$  electrons and a smaller magnetic moment, e.g.,  $\text{Pr}^{3+}$ . In rare-earth ions with fewer  $f$  electrons, the  $4f$  wavefunction is spatially extended [10] and can then be largely overlapped with the O  $2p$  orbitals at the O1 site (Fig. 1 (a)) in the pyrochlore lattice. Besides, for  $\text{Pr}^{3+}$  ions, the magnetic dipolar interaction, which is proportional to the square of the moment size, is reduced by an order of magnitude to 0.1 K between the nearest-neighbor sites, in comparison to that for  $\text{Dy}^{3+}$  ions. Then, the superexchange interaction due to virtual  $f$ - $p$  electron transfers, which provides a source of the quantum nature, is expected to play crucial roles in  $\text{Pr}_2\text{TM}_2\text{O}_7$  ( $\text{TM}$ : a transition metal).

Recent experiments on  $\text{Pr}_2\text{Sn}_2\text{O}_7$  [11],  $\text{Pr}_2\text{Zr}_2\text{O}_7$  [12], and  $\text{Pr}_2\text{Ir}_2\text{O}_7$  [13] have shown that the  $\text{Pr}^{3+}$  ion provides the  $(111)$  Ising moment described by a non-Kramers magnetic doublet. As in the spin ice, any magnetic dipole LRO is absent [11–16].  $\text{Pr}_2\text{Ir}_2\text{O}_7$  shows a metamagnetic transition only when the magnetic field is applied in the  $[111]$  direction [14], indicating the ice-rule formation due

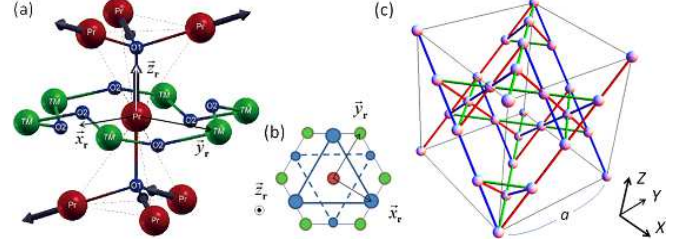


FIG. 1: (Color) (a)  $\text{Pr}^{3+}$  ions (red) form tetrahedrons (dashed lines) centered at  $\text{O}^{2-}$  ions (O1) (blue), and are surrounded by  $\text{O}^{2-}$  ions (O2) (blue) in the  $D_{3d}$  symmetry as well as by  $\text{TM}$  ions (green). Each Pr magnetic moment (bold arrow) points to either of the two neighboring O1 sites. (b) The local coordinate frame  $(\vec{x}_r, \vec{y}_r, \vec{z}_r)$  from the top. Upward and downward triangles of the  $\text{O}^{2-}$  ions (O2) are located above and below the hexagon of the  $\text{TM}$  ions. (c) The Pr pyrochlore lattice. The phase  $\varphi_{r,r'}$  in Eq. (2) depends on the color of the bonds. The global coordinate frame  $(X, Y, Z)$  is also shown.

to a ferromagnetic coupling  $J \sim 1.4$  K [14]. On the other hand, the Curie-Weiss temperature  $T_{CW}$  is antiferromagnetic for the zirconate [12] and iridate [13], unlike the spin ice. The stannate shows a significant level of low-energy short-range spin dynamics [15], which is absent in the classical spin ice. Furthermore, the iridate shows the Hall effect at zero magnetic field without magnetic dipole order [14], suggesting an onset of a chiral spin liquid [3] at a temperature  $\sim J$  due to quantum fluctuations.

In this Letter, we derive the realistic effective model for Pr  $4f$  moments on the pyrochlore lattice. It contains appreciable quantum nature leading to a cooperative ferroquadrupolar ground state, accompanied by crystal symmetry lowering from cubic to tetragonal and a frustration in the chirality ordering. Our scenario explains unusual magnetic properties observed in  $\text{Pr}_2\text{TM}_2\text{O}_7$  suggesting a dynamically fluctuating spin ice [14–16].

We start with  $f^2$  configurations for  $\text{Pr}^{3+}$  forming the tetrahedron centered at the  $\text{O}^{2-}$  ion (O1) in  $\text{Pr}_2\text{TM}_2\text{O}_7$  (Fig. 1). The  $LS$  coupling gives the ground-state manifold  ${}^3H_4$ . Each  $\text{Pr}^{3+}$  ion is placed in a crystalline electric field (CEF) which has the  $D_{3d}$  symmetry about the  $\langle 111 \rangle$  direction toward the O1 site. It is useful to define the lo-

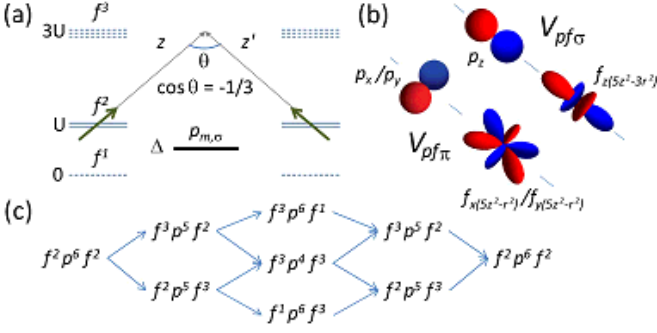


FIG. 2: (Color online) (a) Local level scheme for  $f$  and  $p$  electrons, and the local quantization axes  $\vec{z}_r$  and  $\vec{z}_{r'}$ . (b)  $f$ - $p$  transfer integrals. (c) Virtual hopping processes.  $n$  ( $n'$ ) and  $\ell$  in the state  $f^n p^\ell f^{n'}$  represent the number of  $f$  electrons at the Pr site  $\mathbf{r}$  ( $\mathbf{r}'$ ) and that of  $p$  electrons at the O1 site.

cal quantization axis  $\vec{z}_r$  as this direction, as well as  $x$  and  $y$  axes as  $\vec{x}_r$  and  $\vec{y}_r$  depicted in Figs. 1 (a) and (b). The CEF favors  $J^z = \pm 4$  configurations for the total angular momentum, which are linearly coupled to  $J^z = \pm 1$  and  $\mp 2$  because of the  $D_{3d}$  CEF [18]. This leads to the atomic non-Kramers magnetic ground doublet

$$|\sigma^z\rangle = \alpha|J^z = 4\sigma^z\rangle + \beta\sigma^z|J^z = \sigma^z\rangle - \gamma|J^z = -2\sigma^z\rangle, \quad (1)$$

with small real coefficients  $\beta$  and  $\gamma$  as well as  $\alpha = \sqrt{1 - \beta^2 - \gamma^2}$ . The pseudospin  $\sigma^z = \pm$  represents the direction of the Ising (“in” or “out”) magnetic dipole moment, in contrast to the case of a *nonmagnetic* doublet labeled by the atomic quadrupole moment [19] in materials having other CEF symmetries,  $\text{PrFe}_4\text{P}_{12}$  [20],  $\text{UPt}_3$  [21], and  $\text{UPd}_2\text{Al}_3$  [22]. For  $\text{Pr}_2\text{Ir}_2\text{O}_7$ , the first excited crystal-field level is a singlet located at 168 K and the second is a doublet at 648 K [18]. They are similarly large for  $\text{Pr}_2\text{Sn}_2\text{O}_7$  [15]. These energy scales are two orders of magnitude larger than our relevant energy scale  $J \sim 1.4$  K. Hence we neglect these CEF excitations.

Now we derive the effective Hamiltonian through the fourth-order strong-coupling perturbation theory. Virtual local  $f^1$  and  $f^3$  states have an energy gain of the Coulomb repulsion  $U$  and cost of  $2U$ , respectively (Fig. 2 (a)), where the  $LS$  coupling has been ignored in comparison with  $U$ . Creating a virtual  $p$  hole decreases the energy by the  $p$  electron level  $\Delta$  compared with the  $f^1$  level. The  $f$ - $p$  electron transfer is allowed only within the orbital  $l_z = 0$  and  $\pm 1$  manifolds, whose amplitudes are given by Slater-Koster parameters  $V_{pf\sigma}$  and  $V_{pf\pi}$  [23], respectively (Fig. 2 (b)). The local coordinate frames for the nearest-neighbor Pr sites are crucially different; for instance,  $\vec{z}_r \cdot \vec{z}_{r'} = -1/3$ . The perturbation expansion in  $V_{pf\sigma}$  and  $V_{pf\pi}$  is then carried out by taking into account the different local coordinate frames and the virtual processes (Fig. 2 (c)). The projection of this superexchange Hamiltonian onto the subspace of doublets (Eq. (1)) leads

to the pseudospin-1/2 Hamiltonian;

$$\begin{aligned} H_{\text{eff}} = J \sum_{\langle \mathbf{r}, \mathbf{r}' \rangle}^{\text{n.n.}} & [\sigma_{\mathbf{r}}^z \sigma_{\mathbf{r}'}^z + 2\delta (\sigma_{\mathbf{r}}^+ \sigma_{\mathbf{r}'}^- + \sigma_{\mathbf{r}}^- \sigma_{\mathbf{r}'}^+)] \\ & + 2q (e^{i\varphi_{\mathbf{r}, \mathbf{r}'}} \sigma_{\mathbf{r}}^+ \sigma_{\mathbf{r}'}^+ + h.c.), \end{aligned} \quad (2)$$

with  $\sigma_{\mathbf{r}}^{\pm} \equiv (\sigma_{\mathbf{r}}^x \pm i\sigma_{\mathbf{r}}^y)/2$  and  $(\sigma_{\mathbf{r}}^x, \sigma_{\mathbf{r}}^y, \sigma_{\mathbf{r}}^z) = \vec{\sigma}_{\mathbf{r}} \cdot (\vec{x}_{\mathbf{r}}, \vec{y}_{\mathbf{r}}, \vec{z}_{\mathbf{r}})$ , where  $\vec{\sigma}_{\mathbf{r}}$  represents the Pauli matrix for the pseudospin at the site  $\mathbf{r}$ . We have adopted the simplest gauge where the phase  $\varphi_{\mathbf{r}, \mathbf{r}'}$  takes 0,  $2\pi/3$ ,  $-2\pi/3$  depending on the color of the bond directions shown in Fig. 1 (c), by rotating the  $x$  and  $y$  axes by  $\pi/12$  from those shown in Figs. 1 (a) and (b). This phase can not be fully gauged away, because of the noncollinearity of the  $\langle 111 \rangle$  magnetic moments and the three-fold rotational invariance of  $(\mathbf{r}, \vec{\sigma}_{\mathbf{r}})$  about the  $[111]$  axes. Only  $\sigma_{\mathbf{r}}^z$  contributes to the *magnetic dipole moment*  $J_{\mathbf{r}}^z$ , while  $\sigma_{\mathbf{r}}^{x,y}$  the *atomic quadrupole moment*  $J_{\mathbf{r}}^x, J_{\mathbf{r}}^y$ , as can be shown by direct calculations. For a realistic case  $-0.37 \lesssim V_{pf\pi}/V_{pf\sigma} \lesssim -0.02$ , the Ising coupling  $J$  between the nearest-neighbor pseudospins is found to be positive, i.e., antiferroic. This indicates the “ferromagnetic” coupling between the nearest-neighbor  $4f$  magnetic moments because of the tilting of the local  $z$  axes,  $\vec{z}_r \cdot \vec{z}_{r'} = -1/3$ . Then, it can provide a source of the ice-rule formation. The  $D_{3d}$  CEF creates two additional quantum-mechanical interactions; the pseudospin-exchange and pseudospin-nonconserving terms. Their coupling constants  $\delta$  and  $q$  are insensitive to  $U/V_{pf\sigma}$  and  $\Delta/V_{pf\sigma}$  but strongly depends on  $\beta$  and  $\gamma$ . Figure 3 (a) shows  $\delta$  and  $q$  as functions of  $\beta$  for the trigonal CEF with by keeping the ratio  $\gamma/\beta = 3$ . Henceforth, we adopt rough estimates  $U/V_{pf\sigma} = 5$ ,  $\Delta/V_{pf\sigma} = 4$ , and  $V_{pf\pi}/V_{pf\sigma} = -0.3$  from first-principles calculations (published elsewhere), and  $\beta = 7.5\%$  and  $\gamma = 3\beta$  from the CEF analysis based on inelastic neutron-scattering experiments [18]. Then, we obtain  $\delta \sim 0.51$  and  $q \sim 0.89$ , indicating the appreciable quantum nature. The two couplings play crucial roles in inducing a cooperative ferroquadrupolar order instead of the classical spin ice [8] or the  $U(1)$  spin liquid [24].

A mean-field analysis [5] on Eq. (2) yields two distinct states. (i) Magnetic dipolar states characterized by a nonzero  $\langle \sigma_{\mathbf{r}}^z \rangle$  have the lowest energy  $-2J$  per tetrahedron at the wavevector  $\mathbf{q} = \frac{2\pi}{a}(hhl)$  with  $a$  being the side length of the unit cube (Fig. 1 (c)). (ii) A quadrupolar state with a nonzero  $\langle \sigma_{\mathbf{r}}^{x,y} \rangle$  has the energy  $-2(\delta + 2q)J$  at  $\mathbf{q} = 0$  for  $\delta, q > 0$ . Thus, for  $\delta + 2q > 1$  as in our case, the atomic quadrupole moment  $\sigma_{\mathbf{r}}^{x,y}$  should form the LRO *without any dipole LRO*. However, we will show below that the ground state is further replaced with a cooperative ferroquadrupolar state because of the quantum interplay between atomic dipoles  $\sigma_{\mathbf{r}}^z$  and quadrupoles  $\sigma_{\mathbf{r}}^{x,y}$ .

First let us solve Eq. (2) on a single tetrahedron. The similar analysis on a distinct model for  $\text{Tb}_2\text{Ti}_2\text{O}_7$  [25] has been employed to discuss the RVB-singlet quantum spin ice [26]. With increasing  $\beta$  and thus  $\gamma$  from

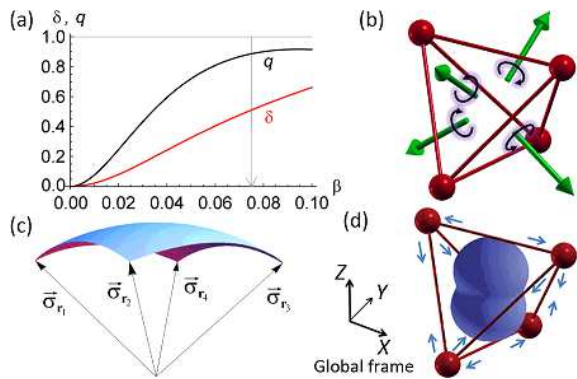


FIG. 3: (Color online) (a) Coupling constants  $\delta$  and  $q$  versus  $\beta (= \gamma/3)$ . The arrow points to the experimentally estimated value of  $\beta$  [18]. (b) Outward normal vectors (green arrows) of the surfaces of the tetrahedron, used to define the chirality  $\kappa_T$ . (c) Solid angle subtended by four pseudospins  $\vec{\sigma}_{r_i}$ . (d) Distribution of the tetrahedral magnetic moment  $\vec{M}_T$  in the cooperative ferroquadrupolar state ( $\langle Q_T^{ZZ} \rangle > 0$ ). The arrows represent the lattice deformation linearly coupled to  $Q_T^{ZZ}$ .

0, three classical levels corresponding to the “2-in, 2-out”, “3-in, 1-out”/“1-in, 3-out” ( $\Delta E = 2J$ ), and “4-in”/“4-out” ( $\Delta E = 8J$ ) configurations are split to three doublets, three triplets, and one singlet. In our case, the ground-state manifold has the  $E_g$  symmetry with the double degeneracy  $\chi = \pm$  as described as  $|\Psi_\chi^s\rangle = \frac{c_2}{\sqrt{6}} \sum_{\tau=\pm} (e^{i\frac{2\pi}{3}\chi} |\tau X\rangle + e^{-i\frac{2\pi}{3}\chi} |\tau Y\rangle + |\tau Z\rangle) + c_4 |4\chi\rangle$  with real coefficients  $c_2$  and  $c_4$ . Here, the orthonormal state  $|+4\rangle/|-4\rangle$  represents the “4-in”/“4-out” configuration, while  $|\pm X\rangle$ ,  $|\pm Y\rangle$ , and  $|\pm Z\rangle$  denote the “2-in, 2-out” having the net magnetic dipole moment  $\vec{M}_T = M_0 \sum_{\mathbf{r}} \sigma_{\mathbf{r}}^z \hat{z}_{\mathbf{r}}$ , pointing to the  $\pm X$ ,  $\pm Y$ , and  $\pm Z$  directions of the global coordinate frame, respectively. We have introduced the moment amplitude  $M_0 = gJ\mu_B(4\alpha^2 + \beta^2 - 2\gamma^2) \approx 2.9\mu_B$  with the Landé factor  $g_J = 4/5$ . The sign  $\chi = \pm$  represents the net pseudospin chirality of the tetrahedron,  $\kappa_T = \frac{1}{2} \sum_{\mathbf{r}_1, \mathbf{r}_2, \mathbf{r}_3} \vec{\sigma}_{\mathbf{r}_1} \cdot \vec{\sigma}_{\mathbf{r}_2} \times \vec{\sigma}_{\mathbf{r}_3}$ , through the relation  $\langle \Psi_\chi^s | \kappa_T | \Psi_{\chi'}^s \rangle = \sqrt{3}c_2^2 \chi \delta_{\chi, \chi'}$ . Here, the summation over the sites  $\mathbf{r}_1, \mathbf{r}_2, \mathbf{r}_3$  on the tetrahedron  $T$  is taken so as they appear counterclockwise about the outward normal to the plane spanned by the three sites (Fig. 3 (b)). This  $\kappa_T$  gives the solid angle subtended by the four pseudospins (Fig. 3 (c)). Note that the “2-in, 2-out” singlet state with the  $A_{1g}$  symmetry [26],  $\sum_{\tau=\pm} (|\tau X\rangle + |\tau Y\rangle + |\tau Z\rangle)/\sqrt{6}$ , is located at a high energy  $\Delta E \sim 7J$ . The triply degenerate first excited states consist of only “3-in, 1-out” and “1-in, 3-out”, and are located at  $\Delta E \sim J$ . In fact, any eigenstate of the single-tetrahedron Hamiltonian is described by either “3-in, 1-out” and “1-in, 3-out” configurations or “2-in, 2-out” and “4-in”/“4-out” configurations. Therefore, quantum effects of creating “3-in, 1-out” and “1-in, 3-out” configurations from the “2-in, 2-out” can not be taken into

account in the single-tetrahedron analysis.

To overcome this drawback, we numerically solve the model for the 16-site ( $N = 16$ ) cubic cluster with the periodic boundary condition (Fig. 1 (c)). It is found that the ground states have a six-fold degeneracy labeled by the inversion ( $I$ ) even(+)/odd(-) and the wavevector  $\mathbf{k}_X = (\frac{2\pi}{a}, 0, 0)$ ,  $\mathbf{k}_Y = (0, \frac{2\pi}{a}, 0)$ , or  $\mathbf{k}_Z = (0, 0, \frac{2\pi}{a})$  with the energy  $\sim -8.825J$  per tetrahedron. The states associated with  $\mathbf{k}_i$  have a cooperative quadrupole moment defined on each tetrahedron,  $\langle Q_T^{ii} \rangle = 0.0387M_0^2$ , where  $Q_T^{ij} = 3M_T^i M_T^j - \vec{M}_T^2 \delta_{ij}$  with  $i, j = X, Y, Z$ . Namely, the net magnetic moment  $\vec{M}_T$  in each tetrahedron  $T$  points, for instance, to the  $\pm Z$  directions with a higher probability than to the  $\pm X$  and  $\pm Y$  (Fig. 3 (d)). Such ferroquadrupole order spontaneously breaking the three-fold rotational invariance about the  $[111]$  axes can occur in the thermodynamic limit. This ferroquadrupole moment  $Q_T^{ii}$  linearly couples to a lattice vibration: the four ferromagnetic bonds and the two antiferromagnetic bonds should be shortened and expanded, respectively, leading to a crystal symmetry lowering from cubic to tetragonal accompanied by a compression in the direction of the ferroquadrupole moment (Fig. 3 (d)). This state shows both axial alignments of magnetic dipoles and a broken translational symmetry, and can then be classified into a magnetic analog of a smectic (or crystalline) phase of liquid crystals [17]. Such magnetic quadrupole correlations in  $\text{Pr}_2\text{TM}_2\text{O}_7$  could be probed by NMR experiments.

Next, we calculate the magnetic dipole correlation,  $S(\mathbf{q}) = \frac{M_0^2}{N} \sum_{\mathbf{r}, \mathbf{r}'} \sum_{i, j} (\delta_{ij} - \frac{q_i q_j}{|\mathbf{q}|^2}) z_{\mathbf{r}}^i z_{\mathbf{r}'}^j \langle \sigma_{\mathbf{r}}^z \sigma_{\mathbf{r}'}^z \rangle_{\text{ave}} e^{i\mathbf{q} \cdot (\mathbf{r} - \mathbf{r}')}$ , averaged over the six-fold degenerate ground states. This quantity is relevant to the neutron-scattering intensity integrated over the low-energy region below the crystal-field excitations from the atomic ground doublet Eq. (1). Note that neutron spins do not couple to  $\sigma_{\mathbf{r}}^\pm$  which represents the atomic quadrupole. Figure 4 (a) shows the profile of  $S(\mathbf{q})$  for  $\mathbf{q} = \frac{2\pi}{a}(hhl)$ . It exhibits intense peaks at (001) and (003), weaker peaks at  $(\frac{3}{4}\frac{3}{4}0)$ , and the minimum at (000), as in the dipolar spin ice [8], though the peaks are broadened by the quantum fluctuations in this ferroquadrupolar state. Besides, the nonzero  $q$  term in the Hamiltonian partially violates the ice rule and eliminates the pinch-point singularity [27, 28] observed at (111) and (002) in the spin ice [29], which should be examined by large system-size calculations. Note that our magnetic profile reproduces powder neutron-scattering results on  $\text{Pr}_2\text{Sn}_2\text{O}_7$  [15] that reveal the enhanced low-energy short-ranged intensity at  $q \sim \frac{2\pi}{a} \sim 0.5 \text{ \AA}^{-1}$  with a shoulder at  $q \sim \frac{6\pi}{a}$  (Fig. 4(b)). This experiment also shows a saturation of the quasielastic peak width  $\sim 0.1 \text{ meV} \sim J$  at 0.2 K [15]. Such large spin relaxation rate can be attributed to the appreciable quantum nature; large  $\delta$  and  $q$  in Eq. (2). These agreements support our scenario of the quantum melting of a spin ice.

Now we concentrate on the ground states having the

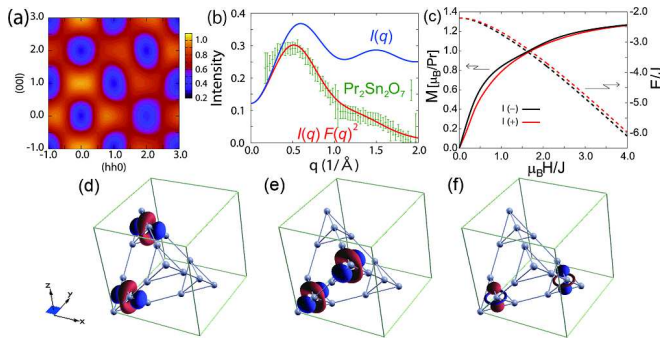


FIG. 4: (Color) (a)  $S(\mathbf{q})/M_0^2$  constructed from the local, nearest-neighbor, and second-neighbor correlations. (b) The theoretical curve (red)  $I(q)F(q)^2$  with the form factor  $F(q)$  and the experimental data (green) of the powder neutron-scattering intensity on  $\text{Pr}_2\text{Sn}_2\text{O}_7$  at 1.4 K [15].  $I(q)$  (blue curve) is the angle average of  $S(\mathbf{q})/M_0^2$ . (c) The magnetizations (left) and energies (right) per site for the  $I$ -odd(-) ground state and the  $I$ -even(+) state under the magnetic field  $\vec{H} \parallel \langle 111 \rangle$ . (d-f) Quadrupole correlations  $\langle Q_T^{ii} Q_{T'}^{jj} \rangle$  between the tetrahedrons  $T$  and  $T'$  displaced by  $\mathbf{r} = \mathbf{r}_X$  (d),  $\mathbf{r}_Y$  (e), and  $\mathbf{r}_Z$  (f) in the cooperative ferroquadrupolar state with the wavevector  $\mathbf{k}_Z$  and  $\langle Q_T^{ZZ} \rangle \neq 0$ . The matrix  $\langle Q_T^{ii} Q_{T'}^{jj} \rangle$  in  $i, j$  has been diagonalized to yield two orthogonal forms of quadrupoles,  $\mathcal{Q}_{r\mu} = \sum_i \lambda_{r\mu}^i Q_T^{ii}$  ( $\mu=1,2$ ). The shape of  $\mathcal{Q}_{r1}$  showing the dominant correlation amplitude is shown. Red/blue regions represent positive/negative values of  $\mathcal{Q}_{r1}$ .

quadrupole moment  $\langle Q_T^{ZZ} \rangle > 0$  and the associated wavevector  $\mathbf{k}_Z$ . The magnetic susceptibility is finite in the ferroquadrupolar state, as seen from the slope of the magnetization curve along the  $\langle 111 \rangle$  direction in Fig. 4 (c). This indicates a negative  $T_{CW}$  as found in  $\text{Pr}_2\text{Zr}_2\text{O}_7$  [12] and  $\text{Pr}_2\text{Ir}_2\text{O}_7$  [14], and the absence of an internal magnetic field as in  $\text{Pr}_2\text{Ir}_2\text{O}_7$  [16]. The magnetic field lifts the degeneracy due to the  $I$  symmetry. The ground-state ( $I$ -odd) magnetization shows a small step or dip around  $\mu_B H/J \sim 1.5$ , in comparison with that of the  $I$ -even excited state. This indicates that the structure develops upon cooling. These agree with the experimental observation on  $\text{Pr}_2\text{Ir}_2\text{O}_7$ ;  $M \sim 0.8\mu_B$  at the metamagnetic transition  $\mu_B H_c/J \sim 1.3$  with  $J \sim 1.4$  K [14].

Finally we spatially resolve the multipolar correlations within the cubic unit cell. Figures 4 (d), (e), and (f) represent quadrupole correlations  $\langle Q_T^{ii} Q_{T'}^{jj} \rangle$  between the tetrahedrons  $T$  and  $T'$  displaced by  $\mathbf{r}_X = (0, \frac{a}{2}, \frac{a}{2})$ ,  $\mathbf{r}_Y = (\frac{a}{2}, 0, \frac{a}{2})$ , and  $\mathbf{r}_Z = (\frac{a}{2}, \frac{a}{2}, 0)$ , respectively. There exist dominant ferroquadrupolar correlations shown in Figs. 4 (d) and (e), both of which favor ferroquadrupole moments along the  $Z$  direction. They prevail over subdominant antiferroquadrupole correlations shown in Fig. 4 (f), and are responsible for the ferroquadrupole order  $\langle Q_T^{ZZ} \rangle \neq 0$ . On the other hand, the chirality correlation  $\langle \kappa_T \kappa_{T'} \rangle$  is weakly ferrochiral between the tetrahedrons shown in Figs. 4 (d) and (e), while it is strongly antiferrochiral between those shown in Fig. 4 (f). This

points to a geometrical frustration suppressing the chirality LRO in each fcc sublattice of the diamond lattice formed by the tetrahedrons. Further studies are required for examining a possibility of a chiral spin liquid [3]. The broken time-reversal symmetry without magnetic dipole LRO, reported in  $\text{Pr}_2\text{Ir}_2\text{O}_7$  [14], might be detected even in insulating magnets such as  $\text{Pr}_2\text{Zr}_2\text{O}_7$  and  $\text{Pr}_2\text{Sn}_2\text{O}_7$  through magneto-optical Kerr-effect measurements.

The proposed scenario of the quantum melting of the spin ice explains magnetic properties observed in  $\text{Pr}_2\text{TM}_2\text{O}_7$ . Effects of coupling of localized  $f$ -electrons to conduction electrons on the transport properties are left for a future study. The orbital motion of conduction electrons can flip the pseudospin-1/2. This could be an origin of the resistivity minimum observed in  $\text{Pr}_2\text{Ir}_2\text{O}_7$  [13].

The authors thank S. Nakatsuji, Y. Machida, Y. B. Kim, K. Matsuhira, and D. MacLaughlin for discussions. The work was supported by Grants-in-Aid for Scientific Research under No. 19052006, 20029006, and 20046016 from the MEXT of Japan and 21740275 from the JSPS.

- 
- [1] P. W. Anderson, Phys. Rev. **102**, 1008 (1956).
  - [2] P. W. Anderson, Mater. Res. Bull. **8**, 153 (1973).
  - [3] X. G. Wen *et al.*, Phys. Rev. B **39**, 11413 (1989).
  - [4] P. A. Lee, Science **321**, 1306 (2009).
  - [5] J. N. Reimers *et al.*, Phys. Rev. B **43**, 865 (1991).
  - [6] M. J. Harris *et al.*, Phys. Rev. Lett. **79**, 2554 (1997).
  - [7] A. P. Ramirez *et al.*, Nature (London) **399**, 333 (1999).
  - [8] S. T. Bramwell and M. J. P. Gingras, Science **294**, 1495 (2001).
  - [9] C. Castelnovo *et al.*, Phys. Rev. Lett. **104**, 107201 (2010).
  - [10] J. Rossat-Mignod, in *Proceedings of the Nato Advanced Study Institute on Systematics and the Properties of the Lanthanides*, Chap. 7, ed. S. P. Sinha (Reidel, Dordrecht, 1983).
  - [11] K. Matsuhira *et al.*, J. Phys. Soc. Jpn. **71**, 1576 (2002).
  - [12] K. Matsuhira *et al.*, J. Phys.: Conf. Series **145**, 012031 (2009).
  - [13] S. Nakatsuji *et al.*, Phys. Rev. Lett. **96**, 087204 (2006).
  - [14] Y. Machida *et al.*, Nature (London) **463**, 210 (2010).
  - [15] H. D. Zhou *et al.*, Phys. Rev. Lett. **101**, 227204 (2008).
  - [16] D. E. MacLaughlin *et al.*, Physica B **404**, 667 (2009).
  - [17] P. G. de Gennes and J. Prost, *The Physics of Liquid Crystals*, 2nd ed. (Clarendon, Oxford, 1993).
  - [18] Y. Machida, Ph. D thesis, Kyoto University (2006).
  - [19] D. L. Cox, Phys. Rev. Lett. **59**, 1240 (1987).
  - [20] Y. Aoki *et al.*, Phys. Rev. B **65**, 064446 (2002).
  - [21] R. Joynt and L. Taillefer, Rev. Mod. Phys. **74**, 235 (2002).
  - [22] A. Grael *et al.*, Phys. Rev. B **46**, (1992) 5818.
  - [23] R. R. Sharma, Phys. Rev. B **19**, 2813 (1979).
  - [24] M. Hermele *et al.*, Phys. Rev. B **69**, 064404 (2004).
  - [25] J. S. Gardner *et al.*, Phys. Rev. Lett. **82**, 1012 (1999).
  - [26] H. R. Molavian *et al.*, Phys. Rev. Lett. **98**, 157204 (2007).
  - [27] S. V. Isakov *et al.*, Phys. Rev. Lett. **93**, 167204 (2004).
  - [28] C. L. Henley, Phys. Rev. B **71**, 014424 (2005).
  - [29] D. J. P. Morris *et al.*, Science **326**, 411 (2009); T. Fennell *et al.*, Science **326**, 415 (2009).